Geophysical Research Letters

RESEARCH LETTER
10.1029/2020GL087036

Key Points:
- We combined ultrafast optics with diamond-anvil cell to study high-pressure thermal conductivity of δ-(Al,Fe)OOH
- Within the spin transition zone the thermal conductivity of δ-(Al,Fe)OOH varies drastically with pressure
- Its exceptionally low thermal conductivity at the lowermost mantle may induce thermal anomalies, altering local thermo-chemical structures

Supporting Information:
- Supporting Information S1

Correspondence to:
W.-P. Hsieh and E. Ohtani,
wphsieh@earth.sinica.edu.tw;
eohtani@tohoku.ac.jp

Citation:
Hsieh, W.-P., Ishii, T., Chao, K.-H., Tsuchiya, J., Deschamps, F., & Ohtani, E. (2020). Spin transition of iron in δ-(Al,Fe)OOH induces thermal anomalies in Earth's lower mantle. *Geophysical Research Letters*, *47*, e2020GL087036. https://doi.org/10.1029/2020GL087036

Received 14 JAN 2020
Accepted 2 FEB 2020
Accepted article online 5 FEB 2020

Spin Transition of Iron in δ-(Al,Fe)OOH Induces Thermal Anomalies in Earth's Lower Mantle

Wen-Pin Hsieh[1,2], Takayuki Ishii[3], Keng-Hsien Chao[1], Jun Tsuchiya[4], Frédéric Deschamps[1], and Eiji Ohtani[5]

[1]Institute of Earth Sciences, Academia Sinica, Taipei, Taiwan, [2]Department of Geosciences, National Taiwan University, Taipei, Taiwan, [3]Bayerisches Geoinstitut, University of Bayreuth, Bayreuth, Germany, [4]Geodynamics Research Center, Ehime University, Matsuyama, Japan, [5]Department of Earth Science, Graduate School of Science, Tohoku University, Sendai, Japan

Abstract Seismic anomalies observed in Earth's deep mantle are conventionally considered to be associated with thermal and compositional anomalies, and possibly partial melt of major lower-mantle phases. However, through deep water cycle, impacts of hydrous minerals on geophysical observables and on the deep mantle thermal state and geodynamics remain poorly understood. Here we precisely measured thermal conductivity of δ-(Al,Fe)OOH, an important water-carrying mineral in Earth's deep interior, to lowermost mantle pressures at room temperature. The thermal conductivity varies drastically by twofold to threefold across the spin transition of iron, resulting in an exceptionally low thermal conductivity at the lowermost mantle conditions. As δ-(Al,Fe)OOH is transported to the lowermost mantle, its exceptionally low thermal conductivity may serve as a local thermal insulator, promoting high-temperature anomalies and the formation of partial melt and thermal plumes at the base of the mantle, strongly influencing thermo-chemical profiles in the region and fate of Earth's deep water cycle.

Plain Language Summary Hydrous minerals subducted to Earth's deep interior may critically affect the thermo-chemical and seismic signatures observed at the bottom of the mantle. We measured thermal conductivity of δ-(Al,Fe)OOH, an important water carrier in deep Earth, to the lowermost mantle pressures. Its thermal conductivity varies drastically across the spin transition of iron and approaches an exceptionally low value of ~5 $W \cdot m^{-1} \cdot K^{-1}$ at the lowermost mantle conditions, much smaller than the pyrolitic mantle. Such anomalous evolution of thermal conductivity would induce anomalies in heat flux and temperature profile in the lower mantle. It could create a local thermal insulating effect that heats up slab's crust at the lowermost mantle, facilitating dehydration melting of surrounding mantle and affecting thermo-chemical features in the region.

1. Introduction

Earth's lowermost mantle features a complex, heterogeneous structure as indicated by seismic velocity anomalies observed in the deep mantle (Garnero & Mcnamara, 2008). However, the origin, nature, and evolution of these anomalies remain inconclusive. Anomalies in either temperature or chemical composition, or their combined effects (Deschamps et al., 2012; Li et al., 2017; McNamara et al., 2010), as likely represented by partial melt or iron enrichments in the major lower-mantle minerals (bridgmanite and ferropericlase), have often been invoked to account for the heterogeneous thermo-chemical signatures and seismic velocity anomalies observed in the large low shear-wave velocity provinces (LLSVPs) and ultralow velocity zones (ULVZs). Though subduction of materials down to the lowermost mantle has also been proposed to influence thermo-chemical structures at least locally (Andrault et al., 2014; Dobson & Brodholt, 2005), the potential impacts of subducted *hydrous* minerals on the heat flux, temperature distribution, and geodynamics in deep mantle have rarely been investigated.

Transportation of water from Earth's surface to its interior via subduction of hydrous minerals within a slab can play a critical role in affecting physical and chemical properties, as well as evolution of the Earth's mantle (Hirschmann & Kohlstedt, 2012; Jacobsen, 2006; Nestola & Smyth, 2016). Mineral physics experiments showed that, among various hydrous minerals, δ-AlOOH along with phase D and phase H is stable under lower-mantle pressure-temperature (*P-T*) conditions (Duan et al., 2018; Nishi et al., 2014; Ohira et al., 2014; Ohtani et al., 2014; Sano et al., 2008; Shieh et al., 1998). The δ-AlOOH is of particular importance

and expected to be a key water carrier to the deep mantle as it could store large amounts of water and survive in the lowermost mantle region (Duan et al., 2018; Ohira et al., 2014; Sano et al., 2008). Prior studies suggested that although the α-FeOOH and α-AlOOH in the subducting slabs dehydrate at shallower depths (Yoshino et al., 2019), the δ-AlOOH phase can be formed in the crust of a subducting slab via the breakdown of phase Egg, which has been found as inclusions in diamond (see, e.g., Wirth et al., 2007, and references therein), and transported to the deep mantle. In the past decades, many physical properties of δ-AlOOH, including crystal symmetry, elastic constants and sound velocities, equation of state, and phase diagram, under extreme conditions have been extensively investigated by experimental and computational methods (see, e.g., Duan et al., 2018; Kang et al., 2017; Kuribayashi et al., 2014; Mashino et al., 2016; Ohira et al., 2014; Ohtani et al., 2001; Pillai et al., 2018; Sano et al., 2008; Sano-Furukawa et al., 2008; Suzuki et al., 2000; Tsuchiya & Tsuchiya, 2009, 2011; Tsuchiya et al., 2008; Vanpeteghem et al., 2002). Moreover, a very recent study further showed that iron (Fe)-bearing δ-AlOOH phase can coexist with bridgmanite in a model basaltic composition (Yuan et al., 2019). The presence of Fe^{3+} in δ-AlOOH in the lower mantle induces profound impacts not only on its physical properties but also potentially on the fate of global cycles of water and iron in the deep mantle (Kawazoe et al., 2017; Ohira et al., 2019). A particularly intriguing property, also reported in Fe-bearing deep mantle minerals (Lin et al., 2013), is that when incorporated with iron, a pressure-induced spin transition of iron is observed in δ-(Al,Fe)OOH around 30–45 GPa (Ohira et al., 2019), through which its unit cell volume and sound velocities change drastically.

Thermal conductivity of mantle minerals holds a key to determine the thermal evolution and geodynamics in Earth's interior (Chang et al., 2017; Dalton et al., 2013; Deschamps & Hsieh, 2019; Hsieh et al., 2017, 2018). It was recently suggested that thermal conductivity anomalies in an oceanic crust of a subducting slab induced by the effect of hydration (Chang et al., 2017) or spin transition (Chao & Hsieh, 2019) could trigger temperature anomalies in the subducting slabs and surrounding mantle, altering the stability fields of minerals in the region. Since δ-(Al,Fe)OOH is likely a major hydrous mineral phase that can be subducted to the deep mantle, its thermal conductivity is expected to play a crucial role in influencing deep mantle thermo-chemical profiles and transportation of water to the bottom of the mantle. However, direct and precise measurements of thermal conductivity of mantle minerals under relevant high *P-T* conditions have been very challenging, due to the difficulties of previous experimental techniques at such extreme conditions, and the accuracy of literature data was insufficient. Recent experimental advancements based on the combination of optical pump-probe method with high-pressure diamond-anvil cell (DAC) have enabled precise measurements of thermal conductivity of deep Earth materials at extremely high pressure conditions (Dalton et al., 2013; Hsieh et al., 2009, 2017, 2018; Ohta et al., 2012, 2017; Okuda et al., 2019). More interestingly, very recent studies reveal that the spin state of iron could considerably change the thermal conductivity of an Fe-rich lower-mantle ferropericlase (Hsieh et al., 2018) and $(Fe_{0.78}Mg_{0.22})CO_3$ siderite (Chao & Hsieh, 2019), whereas the impact of spin transition on hydrous δ-(Al,Fe)OOH thermal conductivity has never been investigated. Thermal conductivity of hydrous δ-(Al,Fe)OOH under extreme *P-T* conditions is therefore critically needed since it would bring important insight into the thermal states in subduction zones and surrounding mantle in Earth's deep interior, as well as potential impacts of water cycle on the deep mantle structure and geodynamics. Here we used ultrafast time domain thermoreflectance (TDTR) coupled with DAC to study the lattice thermal conductivity of δ-AlOOH and δ-(Al,Fe)OOH phases to Megabar pressures at room temperature. We found that the thermal conductivity of δ-(Al,Fe)OOH drastically varies by a factor of 2–3 across the spin transition of iron. We also observed an enhanced iron substitution effect in its low-spin state, causing an exceptionally lower thermal conductivity than the surrounding mantle at lowermost mantle conditions, which would in turn induce local temperature and heat flux anomalies above the core-mantle boundary (CMB) and alter the route of deep water cycle.

2. Materials and Experimental Methods

2.1. Sample Synthesis, Characterization, and Preparation

Polycrystals of δ-AlOOH and single crystals of δ-(Al,Fe)OOH with FeOOH content of 3, 12, and 15 mol.%, respectively, were synthesized by using a 1000-ton Kawai-type multi-anvil apparatus at Bayerisches Geoinstitut (see Kawazoe et al., 2017; Ohira et al., 2019 for more details). The polycrystalline samples were identified with a microfocused X-ray diffractometer (Bruker, D8 DISCOVER) with a two-dimensional solid-state detector (VÅNTEC500) and a microfocus source (IμS) of Co-Kα radiation operated at 40 kV and 500 μA.

Some of single crystals were picked up and identified using a Huber four circles single crystal X-ray diffractometer with Mo-Kα radiation operated at 50 kV and 40 mA. Chemical compositions and spatial homogeneity of the δ-(Al,Fe)OOH were analyzed and confirmed using an electron microprobe analyzer (JEOL, JXA-8200). Each δ-AlOOH and δ-(Al,Fe)OOH sample was polished both sides down to a thickness less than ≈15 μm and cut into circular shape with ≈50 μm in diameter using the Scios DualBeam focused-ion beam system. They were coated with ≈90 nm thick Al film and then loaded into a symmetric piston-cylinder diamond anvil cell (DAC) with 200 or 300 μm culets and a Re gasket. A few ruby spheres were also loaded into the DAC as a pressure calibrant via the fluorescence shift (Mao et al., 1986). The sample was compressed by loading silicone oil (CAS No. 63148-62-9 from ACROS ORGANICS) as the pressure medium. The uncertainty of the pressure in our experiments is typically less than 5%. At pressures higher than about 60–70 GPa, the uncertainty was estimated by comparing the pressures derived from the ruby and diamond anvil signals (Akahama & Kawamura, 2004), as well as the pressure gradient within the sample chamber, typically less than 5 GPa, depending on the pressure (see supporting information Figure S1 for examples of the comparison).

2.2. High-Pressure Lattice Thermal Conductivity Measurements

We used TDTR, a well-established ultrafast optical pump-probe metrology, to measure the lattice thermal conductivity of δ-phase samples at high pressure and room temperature. In our TDTR measurements, we split the output of a mode-locked Ti:sapphire oscillator laser with a central wavelength set to 785 nm into pump and probe beams. The pump beam heated up the Al thin film coated on the sample; the probe beam then measured the resulting optical reflectivity change due to the temperature variations as a function of delay time between pump and probe beams. To extract the small signals that represent the thermal transport properties of the sample, the probe beam was synchronous with the 8.7 MHz modulation frequency of the pump beam. The small variations of the reflected probe beam intensity, including the in-phase V_{in} and out-of-phase V_{out} components, were measured by a fast silicon photodiode and lock-in amplifier. More details of the TDTR method were described in literatures (see, e.g., Cahill, 2004; Hsieh et al., 2009).

To determine the lattice thermal conductivity of δ-phase samples, we compared the time dependence of the ratio $-V_{\text{in}}/V_{\text{out}}$ with calculations by a bidirectional heat diffusion model that considers heat flowing into the sample as well as into the pressure medium (Ge et al., 2006; Schmidt et al., 2008). Supporting information Figure S2 presents a set of example data (open symbols) with calculations (red curve) by the heat diffusion model. There are several parameters in the thermal model, such as laser spot size (≈7.6 μm in radius) and thickness, thermal conductivity, and volumetric heat capacity of each layer (i.e., δ-phase sample, Al film, and silicone oil), while the thermal conductivity of the δ-phase sample is the only significant unknown and free parameter to be determined. Detailed mathematical equations for our bidirectional heat diffusion model can be found in Schmidt et al. (2008). We in situ measured the Al film thickness at ambient conditions via picosecond acoustics (O'Hara et al., 2001); however, after the sample is compressed to high pressures the acoustic signals are too weak to be used. Therefore, we estimated the Al film thickness under pressure following a method developed in Chen et al. (2011). Under our experimental conditions where the pump beam is electro-optically modulated at 8.7 MHz, the thermal penetration depths (the skin depth that heat can diffuse into a material) of the δ-phase sample and silicone oil are both on the order of few hundred nanometers only (Hsieh et al., 2009); thus, calculations of the heat diffusion model is insensitive to their thicknesses. The pressure dependences of thermal conductivity and volumetric heat capacity of silicone oil and Al film were taken from literatures (Hsieh, 2015; Hsieh et al., 2009). The volumetric heat capacities of δ-AlOOH and δ-(Al,Fe)OOH at high pressures are described below. We estimated that the uncertainties in all the parameters used in our heat diffusion model would propagate ≈20% error in the derived thermal conductivity of δ-AlOOH and δ-(Al,Fe)OOH below 30 GPa and less than 30% error at ≈100 GPa. Tests of sensitivity of our thermal model to input parameters are shown in supporting information Figure S3.

2.3. Calculations of the Heat Capacity at High Pressures

In order to estimate the heat capacity and the equation of state of δ-AlOOH, we conducted first-principles calculation based on density functional theory. We employed generalized gradient approximation proposed by Perdew Burke and Ernzerhof to describe the exchange correlation functional (Perdew et al., 1996). Electronic wave functions were expanded in plane waves by the use of projector augmented-wave potentials (Blöchl, 1994). We set a kinetic cutoff of 80 Ry for plane wave expansion of the projector augmented-wave

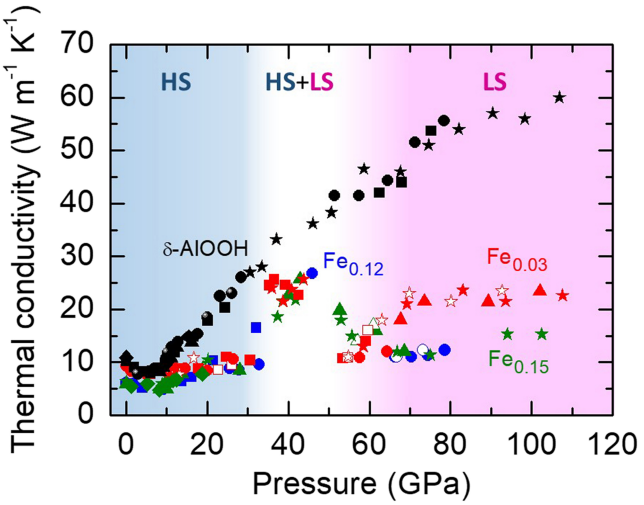

Figure 1. High-pressure lattice thermal conductivity of δ-AlOOH (black symbols), δ-$(Al_{0.97}Fe_{0.03})$OOH ($Fe_{0.03}$, red symbols), δ-$(Al_{0.88}Fe_{0.12})$OOH ($Fe_{0.12}$, blue symbols), and δ-$(Al_{0.85}Fe_{0.15})$OOH ($Fe_{0.15}$, green symbols) phases at room temperature. For each composition, several runs of measurement show consistent results, where each run is represented by one symbol shape with solid symbols for compression and open symbols for decompression cycle, respectively. The experimental uncertainties for the conductivity are typically ≈20% below 30 GPa and ≈30% at 100 GPa. The blue and red shaded areas represent the pressure ranges for the high-spin (HS) and low-spin (LS) state of δ-(Al,Fe)OOH, respectively; the faded region in between shows the spin transition zone with mixed-spin state (HS + LS).

potentials. The structure is fully relaxed at 0, 5, 10, 15, 20, 25, and 30 GPa with space group $P2_1nm$; and 30, 40, 50, 60, 80, and 100 GPa with space group *Pnnm* by the damped variable cell shape molecular dynamics method implemented with Quantum ESPRESSO codes (Giannozzi et al., 2009) until residual forces became less than 1.0×10^{-5} Ry/au. The irreducible Brillouin zone of δ-AlOOH was sampled on $4 \times 4 \times 6$ Monkhorst-pack mesh (Monkhorst & Pack, 1976). After relaxation of the structure, we calculated phonon frequencies of δ-AlOOH using density functional perturbation theory (Baroni et al., 2001). The dynamical matrices are sampled on $4 \times 4 \times 6$ $\boldsymbol{q}$-grid, and then force constant matrices were interpolated on denser meshes in order to obtain the Helmholtz free energy (F) within quasi harmonic approximation

$$F(V,T) = U_0(V) + \frac{1}{V}\sum_{\boldsymbol{q}j} h\omega_j(\boldsymbol{q},V) + k_B T \sum_{\boldsymbol{q}j} \ln\left[1-\exp\left(-\frac{h\omega_{j(\boldsymbol{q},V)}}{k_B T}\right)\right], \quad (1)$$

where the first, second, and third terms are the static lattice, zero-point, and thermal contributions, respectively. Then, thermal property, such as constant pressure heat capacity C_P, is derived from standard thermodynamic relations (Tsuchiya et al., 2005), see supporting information Figure S4 and Table S1 for the pressure dependence of the molar volume and volumetric heat capacity C_P of δ-AlOOH at 300 K.

At 15–30 GPa, thermodynamic properties of δ-AlOOH show anomalous behaviors and we found that quasi harmonic approximation is invalid. This is associated with hydrogen bond symmetrization in δ-AlOOH where the vibrational frequencies anomalously decrease at 15–30 GPa (Tsuchiya et al., 2002, 2008). Except for above pressure range, C_P of δ-AlOOH is almost a constant of ~3 J·cm^{-3}·K^{-1} at 300 K and 0–100 GPa.

First-principles calculations of the heat capacity of δ-(Al,Fe)OOH at high pressures were not performed due to its computational complexity, in particular, across the spin transition. Prior studies on the heat capacity of (Mg,Fe)O indicated that the heat capacity of MgO was slightly modified when adding 12.5 at % iron, that is, the heat capacity of $(Mg_{0.875}Fe_{0.125})O$ is very close to that of MgO (Fukui et al., 2012; Hsieh et al., 2018). As a result, given the relatively small amount of FeOOH (3, 12, and 15 mol %) in δ-AlOOH, in our data analysis we assumed that the volumetric heat capacity of δ-(Al,Fe)OOH with FeOOH contents of 3, 12, and 15 mol % is similar to the δ-AlOOH. We note that the equation of states of δ-(Al,Fe)OOH are very close to that of the δ-AlOOH (Ohira et al., 2019), and eventually with the presence of FeOOH, the actual volumetric heat capacity is expected to be slightly increased due to the higher density, which in turn will lead to a lower derived thermal conductivity. In other words, our derived thermal conductivity of δ-(Al,Fe)OOH (shown as red, blue, and green symbols in Figure 1) is expected to be an upper bound for each of the iron composition

3. Experimental Results: High-Pressure Lattice Thermal Conductivity Across Spin Transition of Iron

Figure 1 shows the lattice thermal conductivity of δ-AlOOH and δ-(Al,Fe)OOH phases at high pressure and room temperature. For each composition, several measurement runs yield consistent results. The thermal conductivity of δ-AlOOH (black symbols in Figure 1) at ambient pressure is 10.9 W·m^{-1}·K^{-1} and slightly decreases with pressure until around 8 GPa, after which it increases rapidly with pressure to around 60 W·m^{-1}·K^{-1} at 107 GPa. Such inflection of thermal conductivity around 8 GPa is presumably caused by the elastic hardening due to the hydrogen bond symmetrization, although its onset pressure was reported to vary slightly among different studies (Cortona, 2017; Kang et al., 2017; Kuribayashi et al., 2014; Mashino et al., 2016; Sano-Furukawa et al., 2009; Tsuchiya & Tsuchiya, 2009; Tsuchiya et al., 2002). Compared to the Fe-free, major lower-mantle phase, $MgSiO_3$ bridgmanite (Hsieh et al., 2017), the thermal

conductivity of δ-AlOOH at deep mantle pressures is about a factor of 2 higher; however, incorporation of iron significantly changes the contrast between these two mineral phases (see our results below).

Interestingly, the presence of iron in δ-AlOOH substantially alters the evolution of thermal conductivity at lower-mantle pressures (see red, blue, and green symbols in Figure 1). With 3 mol % FeOOH in δ-AlOOH, that is, δ-$(Al_{0.97}Fe_{0.03})$OOH (red symbols), the thermal conductivity at ambient conditions is slightly reduced to 9.3 $W{\cdot}m^{-1}{\cdot}K^{-1}$. Similar to δ-AlOOH, the δ-$(Al_{0.97}Fe_{0.03})$OOH thermal conductivity undergoes an inflection around 9–10 GPa, which coincides with the pressure where symmetrization of hydrogen bond in the same Fe-bearing δ-AlOOH samples was recently observed by Ohira et al. (2019). Upon further compression through the spin transition zone, ~30–45 GPa (Ohira et al., 2019), the thermal conductivity drastically increases from 10.4 $W{\cdot}m^{-1}{\cdot}K^{-1}$ at ~30 GPa to 25 $W{\cdot}m^{-1}{\cdot}K^{-1}$ at ~40 GPa, followed by a sudden drop back to 10.6 $W{\cdot}m^{-1}{\cdot}K^{-1}$ at 53 GPa. At higher pressures, the thermal conductivity saturates to around 22.3 $W{\cdot}m^{-1}{\cdot}K^{-1}$ at lowermost mantle pressures.

The thermal conductivities of δ-$(Al_{0.88}Fe_{0.12})$OOH and δ-$(Al_{0.85}Fe_{0.15})$OOH (blue and green symbols in Figure 1, respectively) are similar to each other; at ambient pressure they are further reduced to around 5.8 $W{\cdot}m^{-1}{\cdot}K^{-1}$ due to the strong iron impurity effect with enhanced phonon-defect scattering. Again, their thermal conductivities experience a local minimum of around 5.4 $W{\cdot}m^{-1}{\cdot}K^{-1}$ at ~9–10 GPa, where the symmetrization of hydrogen bond occurs (Ohira et al., 2019) and afterward the increasing elastic constants enhance the thermal conductivities. Through the spin transition zone, we also observed drastic, twofold to threefold variations of thermal conductivity, where their thermal conductivities drop back to ~11 $W{\cdot}m^{-1}{\cdot}K^{-1}$ at ~66 GPa, higher than the pressure for δ-$(Al_{0.97}Fe_{0.03})$OOH (53 GPa). The thermal conductivities then saturate to ~15 $W{\cdot}m^{-1}{\cdot}K^{-1}$ at the lowermost mantle pressures, that is, about a factor of 4 smaller than that of the δ-AlOOH and about 33 and 15% lower than the δ-$(Al_{0.97}Fe_{0.03})$OOH and the (Fe,Al)-bearing bridgmanite (Hsieh et al., 2017), respectively. Note that after the spin transition, thermal conductivities of δ-(Al,Fe)OOH with FeOOH content of 3, 12, and 15 mol % all increase again with pressure. The pressure evolutions are, however, different in the onset pressure and the magnitude of such increase, presumably caused by the different iron content, where higher iron content creates stronger phonon-defect scattering that tend to delay the completion of spin transition (higher onset pressure) as well as to reduce the thermal conductivity (smaller magnitude). Moreover, the impact of iron substitution on the thermal conductivity is significantly enhanced in the low-spin state of δ-(Al,Fe)OOH due to the stronger phonon-defect scattering, similar to that observed in the ferropericlase (Hsieh et al., 2018).

It is noteworthy that the spin-transition-induced anomalous evolution of thermal conductivity of δ-(Al,Fe)OOH is similar to that of the $(Fe_{0.78}Mg_{0.22})CO_3$ siderite (Chao & Hsieh, 2019), where the thermal conductivity varies drastically by few folds across the spin transition. A similar simplified physical model (Chao & Hsieh, 2019; Hsieh et al., 2018) may also be used to qualitatively account for the spin-transition-induced drastic variation of δ-(Al,Fe)OOH thermal conductivity: The presence of iron in δ-AlOOH not only induces the phonon-defect scattering but also the resonant spin-phonon scattering. Upon the spin transition, the effect of resonant spin-phonon scattering diminishes, which enhances the phonon relaxation time and the thermal conductivity. When the spin transition almost completes, however, the reduction of the unit cell volume may substantially shorten the phonon relaxation time, considerably decreasing the thermal conductivity. Further computational and theoretical studies are needed to quantitatively understand the complex physics and anomalous behavior across the spin transition.

Our results in Figure 1 offer a platform to model and constrain the effect of iron on the thermal conductivity of δ-(Al,Fe)OOH at deep mantle conditions, where its iron fraction may vary with depth during subduction. In particular, it has been discussed that there could be a potential iron saturation effect on the thermal conductivity of Fe-bearing minerals, where the thermal conductivity reduces upon the presence of iron, yet saturates when the iron content is larger than a threshold value (Deschamps & Hsieh, 2019; Hsieh et al., 2018). The similar pressure dependence of thermal conductivity of 12 and 15 mol % FeOOH in δ-AlOOH (blue and green symbols in Figure 1, respectively) represents the first experimental evidence indicating the iron saturation effect under extreme pressures and sets a *lower bound* for the thermal conductivity of δ-(Al,Fe)OOH at room temperature and deep mantle pressures, offering better constraints on modeling of its iron composition effect.

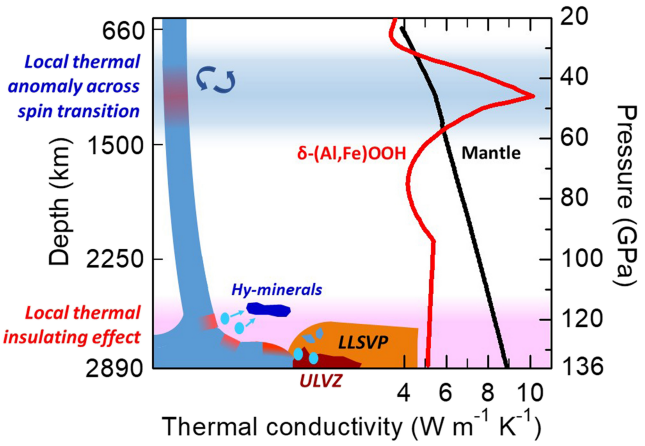

Figure 2. Modeled thermal conductivity of δ-($Al_{0.85}Fe_{0.15}$)OOH (red curve) and pyrolitic mantle (black curve) along a representative geotherm (mantle potential temperature of 2000 K) (Hsieh et al., 2018). A schematic illustration of δ-(Al,Fe)OOH in an oceanic crust of a slab subducted to the bottom of the mantle is also shown. A local thermal anomaly and small-scale convection (illustrated by rotating arrows) due to heterogeneous density distribution could be induced by the spin transition of iron (~30–60 GPa, blue shaded area), where the thermal conductivity of δ-(Al,Fe)OOH varies drastically, resulting in an anomalous temperature distribution within the slab (slab temperature is higher below the region with higher δ-(Al,Fe)OOH thermal conductivity). At the lowermost mantle (pink shaded area), the exceptionally low thermal conductivity of δ-(Al,Fe)OOH creates a local thermal insulating effect that promotes local heating (small red faded regions with higher temperature at the top of the slab) and consequently enhances dehydration. The large amounts of water (light blue droplets) released from δ-(Al,Fe)OOH facilitate partial melting of minerals for seismic ULVZ and also serve as a water source to form deep mantle hydrous minerals (dark blue lobe), for example, hydrous Al-bearing bridgmanite.

4. Discussions and Geophysical Implications

4.1. Potential Local Thermal Anomaly Induced by Spin Transition of Iron

Our findings for the pressure evolution of thermal conductivity of δ-(Al,Fe)OOH and its anomalous behavior across the spin-transition zone offer novel insights into their potential impacts on the thermal state of the deep mantle and subduction zones, as well as on the mechanism driving Earth's deep water cycle. Though the δ-(Al,Fe)OOH phase may not be a major constituent and could be locally populated in the oceanic crust of a subducting slab, its impacts may still be significant, as the effective thermal conductivity of the crustal materials largely depends on how the δ-(Al,Fe)OOH is distributed within the aggregate. When the locally δ-(Al,Fe)OOH-rich crustal material is subducted to depths of approximately 900 to 1,500 km (a depth zone where the spin transition in δ-(Al,Fe)OOH is expected to occur), the drastic variations of thermal conductivity may induce anomalies in the local heat flux and temperature profile within the subducting slab. Yuan et al. (2019) recently showed that in a model composition of hydrous subducting slab, considerable amounts (~9–13 mol %) of FeOOH can be contained in the δ-(Al,Fe)OOH. Moreover, the iron partitioning between the δ-(Al,Fe)OOH and bridgmanite is within the range of 1–3, indicating an Fe-rich composition of δ-(Al,Fe)OOH compared to the bridgmanite. If we assume that the δ-(Al,Fe)OOH contains approximately 12–15 mol % of FeOOH, similar to that observed by Yuan et al. (2019), and its temperature dependence of the lattice thermal conductivity follows a typical $T^{-1/2}$ dependence as many Fe-bearing mantle minerals (Chang et al., 2017; Dalton et al., 2013; Deschamps & Hsieh, 2019; Hsieh et al., 2017, 2018; Klemens et al., 1962; Xu et al., 2004; Zhang et al., 2019), the lattice thermal conductivity of δ-(Al,Fe)OOH at T~2000 K and depths of 900–1,100 km (~30–40 GPa) is expected to rapidly increase from ~4 to 10 W·m^{-1}·K^{-1} (red curve in Figure 2). (The temperature around the interface between a mantle and a subducting slab is expected to be similar.) As a result, the thermal conductivity of δ-(Al,Fe)OOH-rich crustal material would be much larger than that of the surrounding pyrolitic mantle (~5 W·m^{-1}·K^{-1}) (Hsieh et al., 2018), which may in turn enhance the heat transfer between the slab and its surrounding. Such drastic variations of thermal conductivity would induce temperature anomaly within the core of the slab (i.e., beneath the oceanic crust layer), with locally higher (lower) slab core temperature with higher (lower) δ-(Al,Fe)OOH thermal conductivity (see schematic illustration in Figure 2), promoting local heterogeneous density and buoyancy distribution. Differences in the δ-(Al,Fe)OOH content of slabs may then explain, at least partially, differences in the fate of subducting slabs observed by seismology (e.g., Fukao et al., 2001), as slabs enriched in δ-(Al,Fe)OOH may be more buoyant and stack around 1,000 km depth.

4.2. Local Thermal Insulating Effect at the Lowermost Mantle

The base of the lower mantle can be the place where dehydration and hydration of minerals occur: hydrous minerals can dehydrate due to the rapid increase in local temperature above the CMB, and the dehydrated fluid moves upward and serves as the source of hydration that proceeds in the subducting slabs and surrounding mantle. This process enables accumulation of water and hydrous regions at the lowermost mantle. Estimation by VanKeken et al. (2011) suggested that approximately one ocean mass of water could be transported to the deep mantle over the age of the Earth. This amount of water could provide the regions with locally very high water concentration.

As the δ-(Al,Fe)OOH is subducted to the lowermost mantle where it remains stable (Duan et al., 2018; Ohira et al., 2019; Sano et al., 2008), the exceptionally low thermal conductivity could play a key role in affecting the route of water transportation and local thermo-chemical structures at the base of the mantle. Again, assuming its thermal conductivity follows a typical $T^{-1/2}$ dependence, at the lowermost mantle, the

thermal conductivity of δ-(Al,Fe)OOH with 12–15 mol % of FeOOH at T~2400 K before decomposition is expected to be potentially as low as ~5 $W{\cdot}m^{-1}{\cdot}K^{-1}$ (Figure 2), approximately half of the pyrolitic lowermost mantle (~8–10 $W{\cdot}m^{-1}{\cdot}K^{-1}$, for temperatures in the range of 2500 K [~10 $W{\cdot}m^{-1}{\cdot}K^{-1}$]–3500 K [~8 $W{\cdot}m^{-1}{\cdot}K^{-1}$]) (Hsieh et al., 2018). This suggests that when the δ-(Al,Fe)OOH is locally enriched and subducted to the lowermost mantle region and accumulated at the base of the mantle, the δ-(Al,Fe)OOH-rich crustal material serves as a local thermal insulator due to its much lower thermal conductivity compared to the surrounding mantle. The local thermal insulating effect would promote local heating at the base of the mantle and induce lateral heterogeneous heat flow, further influencing the deep mantle and possibly outer core dynamics. Note that if the FeOOH content in δ-(Al,Fe)OOH is depleted, for example, only about 3 mol % of FeOOH, its thermal conductivity at the lowermost mantle conditions would be ~7.5 $W{\cdot}m^{-1}{\cdot}K^{-1}$, which is slightly lower than the pyrolitic lowermost mantle, reducing the effects of local thermal insulation on the heating and geodynamics in the region. However, given the relatively high iron partition coefficient between the δ-(Al,Fe)OOH and bridgmanite, about 1–3 (Yuan et al., 2019), the FeOOH content as low as 3 mol % is expected to be unlikely. The accumulation of the Fe-bearing hydrous mineral, δ-(Al,Fe)OOH, could also account for local heterogeneous thermo-chemical features at the base of the mantle, such as parts of the thermo-chemical structures of LLSVPs, as it may affect the formation and evolution of global deep-seated mantle plumes. In addition, the local increase in temperature induced by the insulating effect of hydrous δ-(Al,Fe)OOH in the crust may further reduce slab's viscosity, such that when reaching the bottom of the mantle the slab could spread more easily around the CMB, with critical consequences on the temporal variations of the CMB heat flux (Deschamps & Li, 2019). Interestingly, Chao and Hsieh (2019) showed that through the spin transition, the thermal conductivity of $(Fe_{0.78}Mg_{0.22})CO_3$ siderite peaks at ~17 $W{\cdot}m^{-1}{\cdot}K^{-1}$ around 45–50 GPa, larger than the δ-$(Al_{0.85}Fe_{0.15})OOH$ (~10 $W{\cdot}m^{-1}{\cdot}K^{-1}$), and then drops down to ~2.5 $W{\cdot}m^{-1}{\cdot}K^{-1}$ in the low-spin state, smaller than the low-spin δ-$(Al_{0.85}Fe_{0.15})OOH$ (~4–5 $W{\cdot}m^{-1}{\cdot}K^{-1}$) at similar P-T conditions. Though the thermal conductivity of $(Fe_{0.78}Mg_{0.22})CO_3$ siderite was measured only up to 67 GPa, if it could also be locally enriched in the crustal material and stably subducted down to the lowermost mantle, the potential presence of $(Fe_{0.78}Mg_{0.22})CO_3$ siderite is expected to enhance both the local thermal anomaly across the spin transition and the local thermal insulating effect at the bottom of the mantle.

Moreover, due to the drastic increase in temperature above the CMB, release of water from the decomposition of δ-AlOOH or δ-(Al,Fe)OOH in this region could facilitate the formation of $FeOOH_x$ (Duan et al., 2018; Yuan et al., 2019) and trigger partial melting of minerals at the base of the mantle, both being proposed to be an origin of the ULVZs (Duan et al., 2018;Liu et al., 2017 ; Yuan et al., 2019). The local thermal insulating effect that additionally raises local temperature in δ-(Al,Fe)OOH due to its exceptionally low thermal conductivity at lowermost mantle would accelerate the dehydration of δ-(Al,Fe)OOH (occurring easier or at shallower depths) and creation of the seismic features for ULVZs (see illustration in Figure 2). One may point out that ULVZs are observed within and at the edges of LLSVPs, not at the foot of slabs (Yu & Garnero, 2018). However, small amounts of slabs may be incorporated within LLSVPs (Li et al., 2014), where dehydration of δ-(Al,Fe)OOH may occur and lead to the formation of ULVZs at the bottom of LLSVPs, again either through the release of water at the bottom of the mantle or through the formation of $FeOOH_x$, a process that would be enhanced if LLSVPs are enriched in iron (Deschamps et al., 2012). In addition, recent first-principles calculations (Muir & Brodholt, 2018) indicate that at the lowermost mantle, high concentration of water (>1,000 ppm) could be incorporated in Al-bearing bridgmanite, creating significant number of vacancies. The large amounts of water released from the enhanced dehydration of δ-(Al,Fe)OOH suggested by our results could serve as a local water source to form the hydrous Al-bearing bridgmanite and pyrite-type $FeOOH_x$ (Liu et al., 2017; Yuan et al., 2019), offering a novel scenario for the potential routes and fate of Earth's deep water cycle.

5. Conclusions

We have coupled ultrafast time-domain thermoreflectance with high-pressure diamond-anvil cell to study the pressure evolution of the lattice thermal conductivity of δ-(Al,Fe)OOH, an important water carrier in deep Earth, to the lowermost mantle pressures. We find that its thermal conductivity varies drastically through the spin transition of iron and approaches an exceptionally low value of ~5 $W{\cdot}m^{-1}{\cdot}K^{-1}$,

approximately half of the surrounding mantle, at the lowermost mantle conditions. At the bottom of the mantle, the low thermal conductivity of δ-(Al,Fe)OOH could induce a locally high temperature anomaly in the crust of a subducting slab, which in turn would promote release of water to the surrounding mantle, leading to the formation of ULVZs observed by seismic data, and strongly influencing local thermo-chemical features and fate of water cycle. Further studies on the thermal conductivity of hydrous minerals that could be present in deep Earth, for example, phase D, phase H, hydrous Al-bearing bridgmanite, and pyrite-type $FeOOH_x$, at deep mantle conditions combined with geodynamics modeling are required to advance our understanding of the complex thermo-chemical structures, origins of the seismic anomalies, and water transportation in deep Earth.

Acknowledgments
This work was partially supported by the Academia Sinica and the Ministry of Science and Technology (MOST) of Taiwan, Republic of China, under Contract AS-CDA-106-M02, 106-2116-M-001-022, and 107-2628-M-001-004-MY3. W. P. H. acknowledges the fellowship from the Foundation for the Advancement of Outstanding Scholarship, Taiwan. T. I. was supported by an Alexander von Humboldt Postdoctoral Fellowship and the German Research Foundation (DFG) (IS350/1-1). J. T. was supported by KAKENHI grants JP15H05834 and JP19H01994. E. O. was supported by KAKENHI grant JP15H05748 and an Alexander von Humboldt research award. We also thank Chao-Chih Chen and Yi-Chi Tsao of Academia Sinica for their help with the experiments. We would like to thank Miyajima of BGI and Shin Ozawa of Tohoku University for their help for preparation of the sample by the focused-ion beam (FIB). Data used for the figures are available at the link https://myspace.sinica.edu.tw/public.php?service=files&t=ca0d524365b0a3eaf4b79a22eb01059e.

References

Akahama, Y., & Kawamura, H. (2004). High-pressure Raman spectroscopy of diamond anvils to 250 GPa: Method for pressure determination in the multimegabar pressure range. *Journal of Applied Physics*, *96*(7), 3748–3751. https://doi.org/10.1063/1.1778482

Andrault, D., Pesce, G., Bouhifd, M. A., Bolfan-Casanova, N., Henot, J.-M., & Mezouar, M. (2014). Melting of subducted basalt at the core-mantle boundary. *Science*, *344*(6186), 892–895. https://doi.org/10.1126/science.1250466

Baroni, S., de Gironcoli, S., Corso, A. D., & Giannozzi, P. (2001). Phonons and related crystal properties from density-functional perturbation theory. *Reviews of Modern Physics*, *134*, 114305. https://doi.org/10.1063/1.3563634

Blöchl, P. (1994). Projecto augmented-wave method. *Physical Review B*, *50*, 17953. https://doi.org/10.1142/9789814365031_0023

Cahill, D. G. (2004). Analysis of heat flow in layered structures for time-domain thermoreflectance. *The Review of Scientific Instruments*, *75*(12), 5119–5122. https://doi.org/10.1063/1.1819431

Chang, Y.-Y., Hsieh, W.-P., Tan, E., & Chen, J. (2017). Hydration-reduced lattice thermal conductivity of olivine in Earth's upper mantle. *Proceedings of the National Academy of Sciences*, *114*(16), 4078–4081. https://doi.org/10.1073/pnas.1616216114

Chao, K.-H., & Hsieh, W.-P. (2019). Thermal conductivity anomaly in (Fe0.78 Mg0.22)CO3 siderite across spin transition of iron. *Journal of Geophysical Research: Solid Earth*, *124*, 1388–1396. https://doi.org/10.1029/2018jb017003

Chen, B., Hsieh, W.-P., Cahill, D. G., Trinkle, D. R., & Li, J. (2011). Thermal conductivity of compressed H_2O to 22 GPa: A test of the Leibfried-Schlömann equation. *Physical Review B*, *83*(13), 132301. https://doi.org/10.1103/PhysRevB.83.132301

Cortona, P. (2017). Hydrogen bond symmetrization and elastic constants under pressure of δ-AlOOH. *Journal of Physics. Condensed Matter*, *29*, 325505. https://doi.org/10.1088/1361-648X/aa791f

Dalton, D. A., Hsieh, W.-P., Hohensee, G. T., Cahill, D. G., & Goncharov, A. F. (2013). Effect of mass disorder on the lattice thermal conductivity of MgO periclase under pressure. *Scientific Reports*, *3*, 2400. https://doi.org/10.1038/srep02400

Deschamps, F., Cobden, L., & Tackley, P. J. (2012). The primitive nature of large low shear-wave velocity provinces. *Earth and Planetary Science Letters*, *349–350*, 198–208. https://doi.org/10.1016/j.epsl.2012.07.012

Deschamps, F., & Hsieh, W.-P. (2019). Lowermost mantle thermal conductivity constrained from experimental data and tomographic models. *Geophysical Journal International*, *219*, S115–S136. https://doi.org/10.1093/gji/ggz231

Deschamps, F., & Li, Y. (2019). Core-mantle boundary dynamic topography: Influence of post-perovskite viscosity. *Journal of Geophysical Research: Solid Earth*, *124*, 9247–9264. https://doi.org/10.1029/2019JB017859

Dobson, D. P., & Brodholt, J. P. (2005). Subducted banded iron formations as a source of ultralow-velocity zones at the core-mantle boundary. *Nature*, *434*(7031), 371–374. https://doi.org/10.1038/nature03430

Duan, Y., Sun, N., Wang, S., Li, X., Guo, X., Ni, H., et al. (2018). Phase stability and thermal equation of state of δ-AlOOH: Implication for water transportation to the deep lower mantle. *Earth and Planetary Science Letters*, *494*, 92–98. https://doi.org/10.1016/j.epsl.2018.05.003

Fukao, Y., Widiyantoro, S., & Obayashi, M. (2001). Stagnant slabs in the upper and lower mantle transition region. *Reviews of Geophysics*, *39*(3), 291–323. https://doi.org/10.1029/1999RG000068

Fukui, H., Tsuchiya, T., & Baron, A. Q. R. (2012). Lattice dynamics calculations for ferropericlase with internally consistent LDA + U method. *Journal of Geophysical Research*, *117*, B12202. https://doi.org/10.1029/2012JB009591

Garnero, E. J., & Mcnamara, A. K. (2008). Structure and dynamics of Earth's lower mantle. *Science*, *320*(5876), 626–628. https://doi.org/10.1126/science.1148028

Ge, Z., Cahill, D., & Braun, P. (2006). Thermal conductance of hydrophilic and hydrophobic interfaces. *Physical Review Letters*, *96*, 186101. https://doi.org/10.1103/PhysRevLett.96.186101

Giannozzi, P., Baroni, S., Bonini, N., Calandra, M., Car, R., Cavazzoni, C., et al. (2009). QUANTUM ESPRESSO: A modular and open-source software project for quantum simulations of materials. *Journal of Physics Condensed Matter*, *21*, 395502. https://doi.org/10.1088/0953-8984/21/39/395502

Hirschmann, M., & Kohlstedt, D. (2012). Water in Earth's mantle. *Physics Today*, *65*(3), 40–45. https://doi.org/10.1063/pt.3.1476

Hsieh, W.-P. (2015). Thermal conductivity of methanol-ethanol mixture and silicone oil at high pressures. *Journal of Applied Physics*, *117*, 235901. https://doi.org/10.1063/1.4922632

Hsieh, W.-P., Chen, B., Li, J., Keblinski, P., & Cahill, D. G. (2009). Pressure tuning of the thermal conductivity of the layered muscovite crystal. *Physical Review B*, *80*, 180302. https://doi.org/10.1103/PhysRevB.80.180302

Hsieh, W.-P., Deschamps, F., Okuchi, T., & Lin, J.-F. (2017). Reduced lattice thermal conductivity of Fe-bearing bridgmanite in Earth's deep mantle. *Journal of Geophysical Research: Solid Earth*, *122*, 4900–4917. https://doi.org/10.1002/2017JB014339

Hsieh, W.-P., Deschamps, F., Okuchi, T., & Lin, J.-F. (2018). Effects of iron on the lattice thermal conductivity of Earth's deep mantle and implications for mantle dynamics. *Proceedings of the National Academy of Sciences of the United States of America*, *115*(16), 4099–4104. https://doi.org/10.1073/pnas.1718557115

Jacobsen, S. D. (2006). Effect of water on the equation of state of nominally anhydrous minerals. *Reviews in Mineralogy and Geochemistry*, *62*, 321–342. https://doi.org/10.2138/rmg.2006.62.14

Kang, D., Feng, Y. X., Yuan, Y., Ye, Q. J., Zhu, F., Huo, H. Y., et al. (2017). Hydrogen-bond symmetrization of δ-AlOOH. *Chinese Physics Letters*, *34*, 108301. https://doi.org/10.1088/0256-307X/34/10/108301

Kawazoe, T., Ohira, I., Ishii, T., Boffa Ballaran, T., McCammon, C., Suzuki, A., & Ohtani, E. (2017). Single crystal synthesis of δ-(Al,Fe)OOH. *American Mineralogist*, *102*(9), 1953–1956. https://doi.org/10.2138/am-2017-6153

Klemens, P. G., White, G. K., & Tainsh, R. J. (1962). Scattering of lattice waves by point defects. *Philosophical Magazine*, *7*(80), 1323–1335. https://doi.org/10.1080/14786436208213166

Kuribayashi, T., Sano-Furukawa, A., & Nagase, T. (2014). Observation of pressure-induced phase transition of δ-AlOOH by using single-crystal synchrotron X-ray diffraction method. *Physics and Chemistry of Minerals*, *41*(4), 303–312. https://doi.org/10.1007/s00269-013-0649-6

Li, M., McNamara, A. K., & Garnero, E. J. (2014). Chemical complexity of hotspots caused by cycling oceanic crust through mantle reservoirs. *Nature Geoscience*, *7*(5), 366–370. https://doi.org/10.1038/ngeo2120

Li, M., McNamara, A. K., Garnero, E. J., & Yu, S. (2017). Compositionally-distinct ultra-low velocity zones on Earth's core-mantle boundary. *Nature Communications*, *8*, 177. https://doi.org/10.1038/s41467-017-00219-x

Lin, J. F., Speziale, S., Mao, Z., & Marquardt, H. (2013). Effects of the electronic spin transitions of iron in lower mantle minerals: Implications for deep mantle geophysics and geochemistry. *Reviews of Geophysics*, *51*, 244–275. https://doi.org/10.1002/rog.20010

Liu, J., Hu, Q., Young Kim, D., Wu, Z., Wang, W., Xiao, Y., et al. (2017). Hydrogen-bearing iron peroxide and the origin of ultralow-velocity zones. *Nature*, *551*(7681), 494–497. https://doi.org/10.1038/nature24461

Mao, H. K., Xu, J., & Bell, P. M. (1986). Calibration of the ruby pressure gauge to 800 kbar under quasi-hydrostatic conditions. *Journal of Geophysical Research*, *91*(B5), 4673. https://doi.org/10.1029/JB091iB05p04673

Mashino, I., Murakami, M., & Ohtani, E. (2016). Sound velocities of δ-AlOOH up to core-mantle boundary pressures with implications for the seismic anomalies in the deep mantle. *Journal of Geophysical Research: Solid Earth*, *121*, 595–609. https://doi.org/10.1002/2015JB012477

McNamara, A. K., Garnero, E. J., & Rost, S. (2010). Tracking deep mantle reservoirs with ultra-low velocity zones. *Earth and Planetary Science Letters*, *299*(1–2), 1–9. https://doi.org/10.1016/j.epsl.2010.07.042

Monkhorst, H. J., & Pack, J. D. (1976). Special points for Brillonin-zone integrations. *Physical Review B*, *13*(12), 5188–5192. https://doi.org/10.1103/PhysRevB.13.5188

Muir, J. M. R., & Brodholt, J. P. (2018). Water distribution in the lower mantle: Implications for hydrolytic weakening. *Earth and Planetary Science Letters*, *484*, 363–369. https://doi.org/10.1016/j.epsl.2017.11.051

Nestola, F., & Smyth, J. R. (2016). Diamonds and water in the deep Earth: A new scenario. *International Geology Review*, *58*(3), 263–276. https://doi.org/10.1080/00206814.2015.1056758

Nishi, M., Irifune, T., Tsuchiya, J., Tange, Y., Nishihara, Y., Fujino, K., & Higo, Y. (2014). Stability of hydrous silicate at high pressures and water transport to the deep lower mantle. *Nature Geoscience*, *7*(3), 224–227. https://doi.org/10.1038/ngeo2074

O'Hara, K. E., Hu, X., & Cahill, D. G. (2001). Characterization of nanostructured metal films by picosecond acoustics and interferometry. *Journal of Applied Physics*, *90*(9), 4852–4858. https://doi.org/10.1063/1.1406543

Ohira, I., Jackson, J. M., Solomatova, N. V., Sturhahn, W., Finkelstein, G. J., Kamada, S., et al. (2019). Compressional behavior and spin state of δ-(Al,Fe)OOH at high pressures. *American Mineralogist*, *104*(9), 1273–1284. https://doi.org/10.2138/am-2019-6913

Ohira, I., Ohtani, E., Sakai, T., Miyahara, M., Hirao, N., Ohishi, Y., & Nishijima, M. (2014). Stability of a hydrous δ-phase, AlOOH-$MgSiO_2(OH)_2$, and a mechanism for water transport into the base of lower mantle. *Earth and Planetary Science Letters*, *401*, 12–17. https://doi.org/10.1016/j.epsl.2014.05.059

Ohta, K., Yagi, T., Hirose, K., & Ohishi, Y. (2017). Thermal conductivity of ferropericlase in the Earth's lower mantle. *Earth and Planetary Science Letters*, *465*, 29–37. https://doi.org/10.1016/j.epsl.2017.02.030

Ohta, K., Yagi, T., Taketoshi, N., Hirose, K., Komabayashi, T., Baba, T., et al. (2012). Lattice thermal conductivity of $MgSiO_3$ perovskite and post-perovskite at the core–mantle boundary. *Earth and Planetary Science Letters*, *349–350*, 109–115. https://doi.org/10.1016/j.epsl.2012.06.043

Ohtani, E., Amaike, Y., Kamada, S., Sakamaki, T., & Hirao, N. (2014). Stability of hydrous phase H $MgSiO_2(OH)_2$ under the lower mantle conditions. *Geophysical Research Letters*, *41*, 8283–8287. https://doi.org/10.1002/2014GL061690

Ohtani, E., Litasov, K., Suzuki, A., & Kondo, T. (2001). Stability field of new hydrous phase, for water transport into the deep mantle. *Geophysical Research Letters*, *28*(20), 3991–3993. https://doi.org/10.1029/2001GL013397

Okuda, Y., Ohta, K., Sinmyo, R., Hirose, K., Yagi, T., & Ohishi, Y. (2019). Effect of spin transition of iron on the thermal conductivity of (Fe, Al)-bearing bridgmanite. *Earth and Planetary Science Letters*, *520*, 188–198. https://doi.org/10.1016/j.epsl.2019.05.042

Perdew, J. P., Burke, K., & Ernzerhof, M. (1996). Generalized gradient approximation made simple. *Physical Review Letters*, *77*(18), 3865–3868. https://doi.org/10.1103/PhysRevLett.77.3865

Pillai, S. B., Jha, P. K., Padmalal, A., Maurya, D. M., & Chamyal, L. S. (2018). First principles study of hydrogen bond symmetrization in δ-AlOOH. *Journal of Applied Physics*, *123*, 115901. https://doi.org/10.1063/1.5019586

Sano, A., Ohtani, E., Kondo, T., Hirao, N., Sakai, T., Sata, N., et al. (2008). Aluminous hydrous mineral δ-AlOOH as a carrier of hydrogen into the core-mantle boundary. *Geophysical Research Letters*, *35*, L03303. https://doi.org/10.1029/2007GL031718

Sano-Furukawa, A., Kagi, H., Nagai, T., Nakano, S., Fukura, S., Ushijima, D., et al. (2009). Change in compressibility of δ-AlOOH and δ-AlOOD at high pressure: A study of isotope effect and hydrogen-bond symmetrization. *American Mineralogist*, *94*(8–9), 1255–1261. https://doi.org/10.2138/am.2009.3109

Sano-Furukawa, A., Komatsu, K., Vanpeteghem, C. B., & Ohtani, E. (2008). Neutron diffraction study of δ-AIOOD at high pressure and its implication for symmetrization of the hydrogen bond. *American Mineralogist*, *93*(10), 1558–1567. https://doi.org/10.2138/am.2008.2849

Schmidt, A., Chiesa, M., Chen, X., & Chen, G. (2008). An optical pump-probe technique for measuring the thermal conductivity of liquids. *The Review of Scientific Instruments*, *79*, 064902. https://doi.org/10.1063/1.2937458

Shieh, S. R., Mao, H. K., Hemley, R. J., & Ming, L. C. (1998). Decomposition of phase D in the lower mantle and the fate of dense hydrous silicates in subducting slabs. *Earth and Planetary Science Letters*, *159*(1–2), 13–23. https://doi.org/10.1016/S0012-821X(98)00062-4

Suzuki, A., Ohtani, E., & Kamada, T. (2000). A new hydrous phase δ-Al00H synthesized at 21 GPa and 1000 °C. *Physics and Chemistry of Minerals*, *27*(10), 689–693. https://doi.org/10.1007/s002690000120

Tsuchiya, J., & Tsuchiya, T. (2009). Elastic properties of δ-AlOOH under pressure: First principles investigation. *Physics of the Earth and Planetary Interiors*, *174*(1–4), 122–127. https://doi.org/10.1016/j.pepi.2009.01.008

Tsuchiya, J., & Tsuchiya, T. (2011). First-principles prediction of a high-pressure hydrous phase of AlOOH. *Physical Review B: Condensed Matter and Materials Physics*, *83*, 054115. https://doi.org/10.1103/PhysRevB.83.054115

Tsuchiya, J., Tsuchiya, T., Tsuneyuki, S., & Yamanaka, T. (2002). First principles calculation of a high-pressure hydrous phase, δ-AlOOH. *Geophysical Research Letters*, *29*(19), 1909. https://doi.org/10.1029/2002gl015417

Tsuchiya, J., Tsuchiya, T., & Wentzcovitch, R. M. (2005). Vibrational and thermodynamic properties of $MgSiO_3$ postperovskite. *Journal of Geophysical Research*, *110*, B02204. https://doi.org/10.1029/2004JB003409

Tsuchiya, J., Tsuchiya, T., & Wentzcovitch, R. M. (2008). Vibrational properties of δ-AlOOH under pressure. *American Mineralogist*, *93*(2–3), 477–482. https://doi.org/10.2138/am.2008.2627

VanKeken, P. E., Hacker, B. R., Syracuse, E. M., & Abers, G. A. (2011). Subduction factory: 4. Depth-dependent flux of H_2O from subducting slabs worldwide. *Journal of Geophysical Research*, *116*, B01401. https://doi.org/10.1029/2010JB007922

Vanpeteghem, C. B., Ohtani, E., & Kondo, T. (2002). Equation of state of the hydrous phase δ-AlOOH at room temperature up to 22.5 GPa. *Geophysical Research Letters*, *29*(7), 22. https://doi.org/10.1029/2001GL014224

Wirth, R., Vollmer, C., Brenker, F., Matsyuk, S., & Kaminsky, F. (2007). Inclusions of nanocrystalline hydrous aluminium silicate "Phase Egg" in superdeep diamonds from Juina. *Earth and Planetary Science Letters*, *259*, 384–399. https://doi.org/10.1016/j.epsl.2007.04.041

Xu, Y., Shankland, T. J., Linhardt, S., Rubie, D. C., Langenhorst, F., & Klasinski, K. (2004). Thermal diffusivity and conductivity of olivine, wadsleyite and ringwoodite to 20 GPa and 1373 K. *Physics of the Earth and Planetary Interiors*, *143*, 321–336. https://doi.org/10.1016/j.pepi.2004.03.005

Yoshino, T., Baker, E., & Duffey, K. (2019). Fate of water in subducted hydrous sediments deduced from stability fields of FeOOH and AlOOH up to 20 GPa. *Physics of the Earth and Planetary Interiors*, *294*, 106295. https://doi.org/10.1016/j.pepi.2019.106295

Yu, S., & Garnero, E. J. (2018). Ultralow velocity zone locations: A global assessment. *Geochemistry, Geophysics, Geosystems*, *19*, 396–414. https://doi.org/10.1002/2017GC007281

Yuan, H., Zhang, L., Ohtani, E., Meng, Y., Greenberg, E., & Prakapenka, V. B. (2019). Stability of Fe-bearing hydrous phases and element partitioning in the system $MgO–Al_2O_3–Fe_2O_3–SiO_2–H_2O$ in Earth' s lowermost mantle. *Earth and Planetary Science Letters*, *524*, 115714. https://doi.org/10.1016/j.epsl.2019.115714

Zhang, Y., Yoshino, T., Yoneda, A., & Osako, M. (2019). Effect of iron content on thermal conductivity of olivine with implications for cooling history of rocky planets. *Earth and Planetary Science Letters*, *519*, 109–119. https://doi.org/10.1016/j.epsl.2019.04.048